IEEE Access
Multidisciplinary : Rapid Review : Open Access Journal

Received January 29, 2019, accepted February 20, 2019, date of publication March 13, 2019, date of current version April 17, 2019.

Digital Object Identifier 10.1109/ACCESS.2019.2904743

Human Head Skin Thickness Modeling for Electromagnetic Dosimetry

ESSAM A. RASHED[1,2,3], (Member, IEEE), JOSE GOMEZ-TAMES[1], (Member, IEEE), AND AKIMASA HIRATA[1], (Fellow, IEEE)

[1]Department of Electrical and Mechanical Engineering, Nagoya Institute of Technology, Nagoya 466-8555, Japan
[2]Department of Computer Science, Faculty of Informatics & Computer Science, The British University in Egypt, Cairo 11837, Egypt
[3]Department of Mathematics, Faculty of Science, Suez Canal University, Ismailia 41522, Egypt

Corresponding author: Essam A. Rashed (essam.rashed@nitech.ac.jp)

This work was supported by the Ministry of Internal Affairs and Communications, Japan.

ABSTRACT In several medical applications as well as human safety evaluation, accurate electromagnetic field exposure assessments are required to identify potential side/adverse effects on humans. Computational human models representing anatomy are commonly used to conduct computational dosimetry studies to assess the *in situ* electric field for quantitative evaluation due to a limitation in conventional human models. The limitation in conventional human models was due to a limited model resolution (typically a few millimeters), which is attributable to the original resolution of medical images. In particular, the importance of the skin layer is suggested in the research agenda of the international standardization body for human electromagnetic exposure. In this paper, we propose a novel method to improve the accuracy of human head skin modeling, which is applicable even to conventional models. To demonstrate the effect of skin modeling on the computed *in situ* electric field, computational dosimetry is conducted for uniform magnetic field exposure as well as transcranial magnetic stimulation. Computational results indicate that the *in situ* electric field for uniform exposure is marginally influenced by the skin thickness and model resolution (up to 5%) for different evaluation metrics used in international safety standards. However, the *in situ* electric field in the skin during transcranial magnetic stimulation and a simulated electrical shaver (non-uniform field exposure) was affected by 11%, which may be worth discussing for optimal brain stimulation considering the side effects of unintended exposure.

INDEX TERMS Skin modeling, TMS, radiation safety, human exposure.

I. INTRODUCTION

For human exposure to non-ionizing radiation, the dominant effect is electrostimulation at frequencies typically lower than 100 kHz and thermal effect at the higher frequencies (< 300 GHz). The border frequencies may vary for the duration of exposure and target tissue, as discussed in the international guidelines/standards for human safety [1], [2]. For electromagnetic field exposure in medical applications and human safety, computational dosimetry becomes an essential tool for estimating internal physical quantities.

At frequencies lower than 100 kHz (referred to as low frequency (LF) hereafter), the *in situ* electric field (EF) is the physical agent for stimulation, so it is an internal physical quantity to be evaluated in compliance with international safety guidelines/standards. However, for LF exposure, there still exists some difficulty in the estimation of the *in situ* EF. For example, in the International Commission on Non-Ionizing Radiation Protection (ICNIRP) guidelines, a reduction factor of 3 is applied to reference level in order to consider numerical uncertainty [1]. The IEEE International Committee on Electromagnetic Safety (ICES) opened the research agenda in LF dosimetry, which is required for future safety standards and is also helpful for medical applications [3]. Especially in the latter, the importance of skin modeling has been suggested as a future direction for investigation.

In humans, the highest *in situ* electric field in the peripheral nervous system is typically observed in the skin. In previous

The associate editor coordinating the review of this manuscript and approving it for publication was Mufti Mahmud.

2169-3536 © 2019 IEEE. Translations and content mining are permitted for academic research only.
Personal use is also permitted, but republication/redistribution requires IEEE permission.
See http://www.ieee.org/publications_standards/publications/rights/index.html for more information.

studies, it has been shown that appropriate modeling of human skin would lead to a better understanding of LF exposure [3]. In medical applications, such as transcranial magnetic stimulation (TMS), sensations and/or pain have been reported simultaneously during brain stimulation sessions [4].

Modeling skin in human phantoms/models refers to the process of identifying skin tissues in a more physically correct representation that simulates real skin thickness and conductivity values. In some studies, skin is modeled as a set of multiple layers, such as dermis, epidermis, and stratum corneum [5]–[7]. Skin modeling in LF dosimetry has been discussed extensively but mostly in terms of human safety standardization. An appropriate assignment of skin conductivity has been discussed for uniform exposure [8]–[10].

Considering skin thickness, the primary reasons for the numerical uncertainties is the stair-casing error, which is inherent to voxel anatomical human body models. The anatomical models are discretized in terms of small voxels, which are suitable for electromagnetic computation with finite difference methods. Some models are based on computer-aided design (CAD) format or discretized in terms of mesh grids for the finite-element method [11], but only a limited number of reports is available for low-computational efficiency. It is known that the computational error becomes largest at the air-tissue (skin) interface in the computational electromagnetics with voxel models [12]. This may also include the discretization error of the human itself or segmentation error because human body models typically have a resolution of a few millimeters.

Measurements of skin thickness have been reported extensively in several publications (see, [13]–[18]). As shown in these papers, the skin thickness is correlated to several parameters, such as race, age, gender, skin type, skin location, health conditions, and daily-base activities. Skin thickness measurements have indicated that actual values may not be effectively expressed with the typical resolution of anatomical models. Human models are presented at millimeter resolutions, which is not suitable to demonstrate the variability of real human skin (in micrometers). Moreover, it is difficult to generate accurate high-resolution models using current clinical medical imaging facilities.

The purpose of the present study is to develop a customized head model in which the skin thickness is fine-tuned from measurements reported in a previous study [13]. Then, the computational dosimetry of the *in situ* electric field is conducted for different exposure scenarios: one loop coil imitating a small source (e.g., electric shavers) and a figure-eight coil used for TMS in addition to uniform magnetic field exposures.

II. MODELS AND METHODS

A. HUMAN MODELS

Pipelines to generate a refined model from original voxel human body models have been proposed and applied to anatomical models developed from MR images [19]. The pipeline is typically composed of the following three procedures: 1) polygonization of conventional low-resolution voxel model, 2) smoothing of polygon model, and 3) voxelization of smoothing polygon model. A smoothed voxel model with an arbitrary resolution can be realized by mediating a polygon model. The first and second steps are almost identical to those presented in [20].

The pipeline described above has the potential to provide a smooth high-resolution human model from low-resolution ones. Through these steps, a new 0.22 mm human model can be generated from an original 2.0 mm one [21]. The skin in the new model is highly smoothed and the discontinuity of the skin layer is highly suppressed. However, the skin thickness accuracy of the resulting model may be still insufficient in many regions. This effect is well-known in the image processing field during the employment of super-resolution processes [22]. The study in [21] uses the Japanese adult male model (TARO) detailed in [23]. The original TARO model, developed by NICT Japan, is of 2.0 mm voxel size, where the skin is represented in almost only a single voxel. Generation of a higher resolution model is likely to produce a skin of uniform thickness all over the model, which would lead to evaluation of electromagnetic dosimetry with additional uncertainty. Without losing generality, in the present study, we will use the TARO model for human head skin modeling. The proposed method, which is detailed below, can also be implemented in other available human models.

B. HEAD SKIN LABELING

For accurate representation of different skin regions in the head, the skin is divided into different regions that have been proved in the literature to have almost uniform thickness. We have divided the TARO head model into 31 different regions using mesh grid vertices as references. The connected vertices of the external head skin layer are classified into one of the 31 regions, as shown in Fig. 1. Every region is assumed to have an almost uniform skin thickness value following the work presented in [13]. The predefined skin thickness values (dermal and epidermal) for the head skin model used in this study are shown in Table 1.

C. SKIN THICKNESS ADJUSTMENT (VOXEL-BASED APPROACH)

The weakness of the procedure discussed in Section II. A is that the model accuracy is highly influenced by the segmentation performed in the original model development. This effect is crucial in small or thin tissues/organs (such as skin). There have only been a few attempts in the literature that aim at measuring/estimating accurate skin thickness [13], [18]. We then proposed two fine-tuning methods of the skin generated using the polygon method with measured data. The first method is a voxel-based computation, and it consists of two main phases: 1) enforcement of skin thickness constraints and 2) minimization of the variation in skin thickness values.

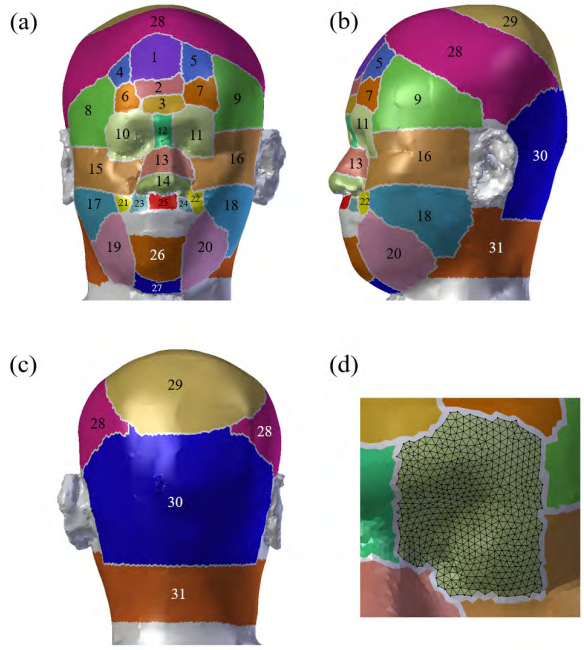

FIGURE 1. Skin labeling of TARO head model. The skin is divided into 31 labeled regions as shown in (a) anterior, (b) lateral, and (c) posterior directions. A mesh grid of region number 11 is shown with magnified view in (d).

TABLE 1. Skin average thickness values obtained from [13] and used to model the different human head regions shown in Fig. 1.

# (r)	Region (Ω_r)	Thickness in mm (t_r)
1	Upper Medial Forehead	1.246
2	Lower Medial Forehead	1.222
3	Glabella	1.386
4 & 5	Upper Lateral Forehead	1.297
6 & 7	Lower Lateral Forehead	1.212
8 & 9	Mid-Nasal Sidewall	1.795
10 & 11	Eyelid	1.230
12	Upper Nasal Dorsum	1.528
13	Lower Nasal Sidewall	2.016
14	ALA	1.993
15 & 16	Malar	1.086
17 & 18	Lower Cheek	1.336
19 & 20	Marionette Fold	1.030
21 & 22	Nasolabial Fold	1.299
23 & 24	Upper Lip	1.496
25	Philtrum	1.244
26	Chin	1.211
27	Anterior Neck	1.278
28	Temporal Scalp	1.383
29	Vertex	0.957
30	Posterior Scalp	1.479
31	Posterior Neck	1.474

In the first phase, a set of prior knowledge obtained from real thickness measurements, as shown in Table 1, are used to adjust realistic skin thickness values in different regions. If the voxelized human model is defined as Γ with the subset Γ_{skin} defining the voxels that identify the skin, the first phase is implemented using the following constraints:

$$\Delta|_{p(i,j,k)} = t_r \quad \forall p(i,j,k) \in \Gamma_{skin} \text{ and } p(i,j,k) \in \Omega_r, \qquad (1)$$

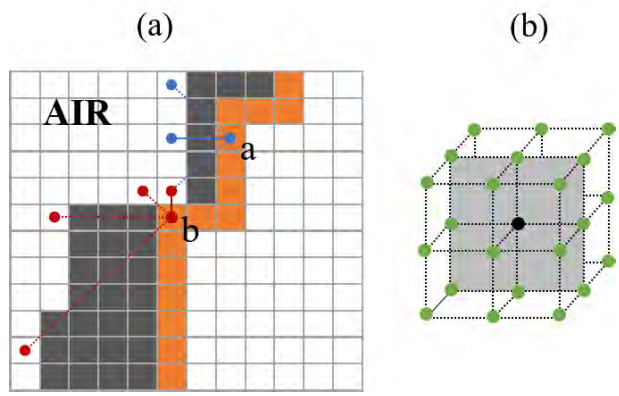

FIGURE 2. Illustration of skin thickness computation process. (a) Orange pixels represent dermal skin layer (unchanged). Blue and red lines identify the potential paths to reach air pixels starting from pixels "a" and "b", respectively. Solid lines represent the shortest path (Δ) at each dermal pixel. For simplicity, (a) is displayed in 2D (8 possible directions per pixel), but actual computations are done in 3D (26 possible directions per voxel, as shown by green circles in (b)).

where $p(i,j,k)$ is a single voxel, Δ is the skin thickness, and t_r is the skin thickness value for the defined region Ω_r, $r = 1, \ldots, 31$. To identify the value of Δ within the voxel representation, we first identify the most interior voxels as the skin dermal layer and compute the value of Δ as the minimum distance to reach an air-representing voxel, as shown in Fig. 2. The first phase is implemented by adding/removing voxels representing skin from the epidermal layer (i.e., external skin) to satisfy the skin thickness constraints. The following algorithm identify the adding/removing voxel process:

for $r = 1, 2, \ldots$ **do**
  forall the $p \in \Omega_r^{der}$ **do**
    $\hat{d} = \arg\min_d dist(p, d)$;
    $\Delta = dist(p, \hat{d})$;
    if $\Delta > t_r$ **then**
      $n = \lfloor (\Delta - t_r)/\epsilon \rfloor$;
      remove n voxels from direction $\hat{d}$;
    end
    if $\Delta < t_r$ **then**
      $n = \lceil (t_r - \Delta)/\epsilon \rceil$;
      add n voxels to direction $\hat{d}$;
    end
  end
end

where Ω_r^{der} defines a dermal skin region, ϵ is the voxel size, and $dist(p, d)$ is the Cartesian distant from voxel p to the first air voxel in direction d. The computed model results from the implementation of constraints in (1) are expected to produce strong stair-case artifacts, which are handled through the second phase.

In the second phase, the total-variation (TV) minimization filter is used to reduce the artifacts generated from phase one. TV minimization is a well-known image processing

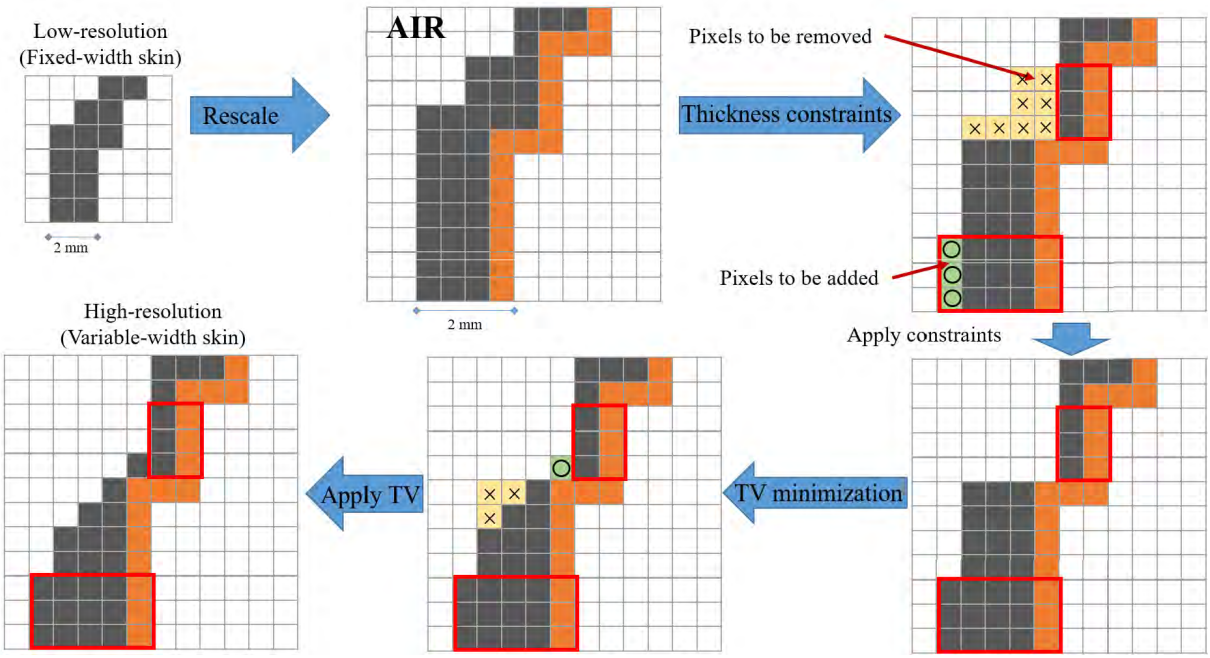

FIGURE 3. Voxel-based skin modeling. From a low-resolution model, direct rescaling will generate a uniform skin thickness. Thickness constraints identify the accurate thickness in each region, which leads to strong stair-case artifacts. The TV minimization filter reduces the artifacts and leads to smooth and more realistic skin modeling without losing thickness constraints. Demonstration is displayed in 2D for simplicity, but actual computations are done in 3D.

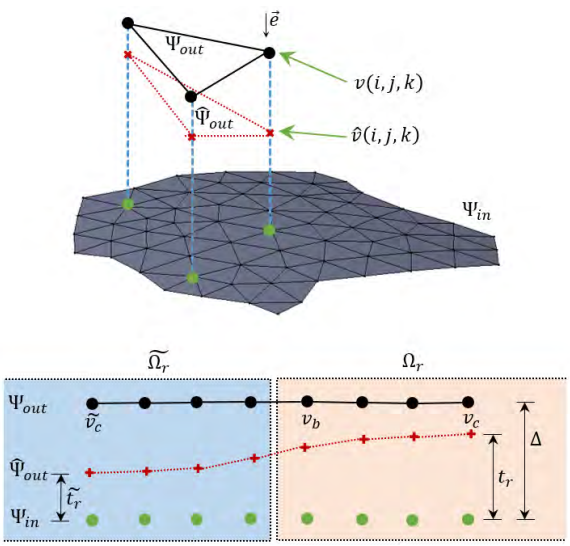

FIGURE 4. A sketch demonstrating the vertex position change to model the skin thickness. Black circles represent the vertices of the original external surface of the skin (Ψ_{out}), which are modeled to the red cross points ($\hat{\Psi}_{out}$). The change in distance is subject to the position of the vertex corresponding to the defined region Ω_r. Skin thickness change in peripheral vertices is different from internal ones. Below is a 2D sketch to demonstrate the transition at peripheral vertices.

technique that aims to globally reduce the variation in image pixel values with superior quality compared to conventional techniques such as mean/median filters [24]. Commonly, TV is implemented to change the pixel values that represent a physical phenomenon used to generate the image, such as light intensity in nature images and attenuation coefficients in x-ray imaging. However, the TV filter here is used to change the skin thickness (i.e., the number of voxels that represent skin thickness) such that the skin thickness is modeled in a more realistic manner. The TV minimization is implemented as follows:

$$\begin{aligned} \min\ TV(\Gamma) &= \sum_{i,j,k} \sqrt{D_x + D_y + D_z}, \\ D_x &= (\Delta|_{p(i,j,k)} - \Delta|_{p(i-1,j,k)})^2, \\ D_y &= (\Delta|_{p(i,j,k)} - \Delta|_{p(i,j-1,k)})^2, \\ D_z &= (\Delta|_{p(i,j,k)} - \Delta|_{p(i,j,k-1)})^2, \end{aligned} \tag{2}$$

where D_x, D_y, and D_z are the skin thickness variation over the x, y, and z axes, respectively. The minimization of (2) is achieved using Chambolle's algorithm described in [25].

In other words, the implementation of TV minimization in (2) aims at finding the values of skin thickness (Δ) at each model voxel ($p(i,j,k) \in \Gamma_{skin}$) such that the variation from measurements in neighbor voxels is minimized globally. This filter is expected to enforce skin thickness variation in a smooth way without losing the thickness constraints applied in the first phase, which present a more realistic modeling of the skin. A simple step-by-step example illustrating the proposed approach is shown in Fig. 3.

D. SKIN THICKNESS ADJUSTMENT (MESH GRID-BASED APPROACH)

A major drawback with the voxel-based modeling is that the computation cost becomes notably high when the model

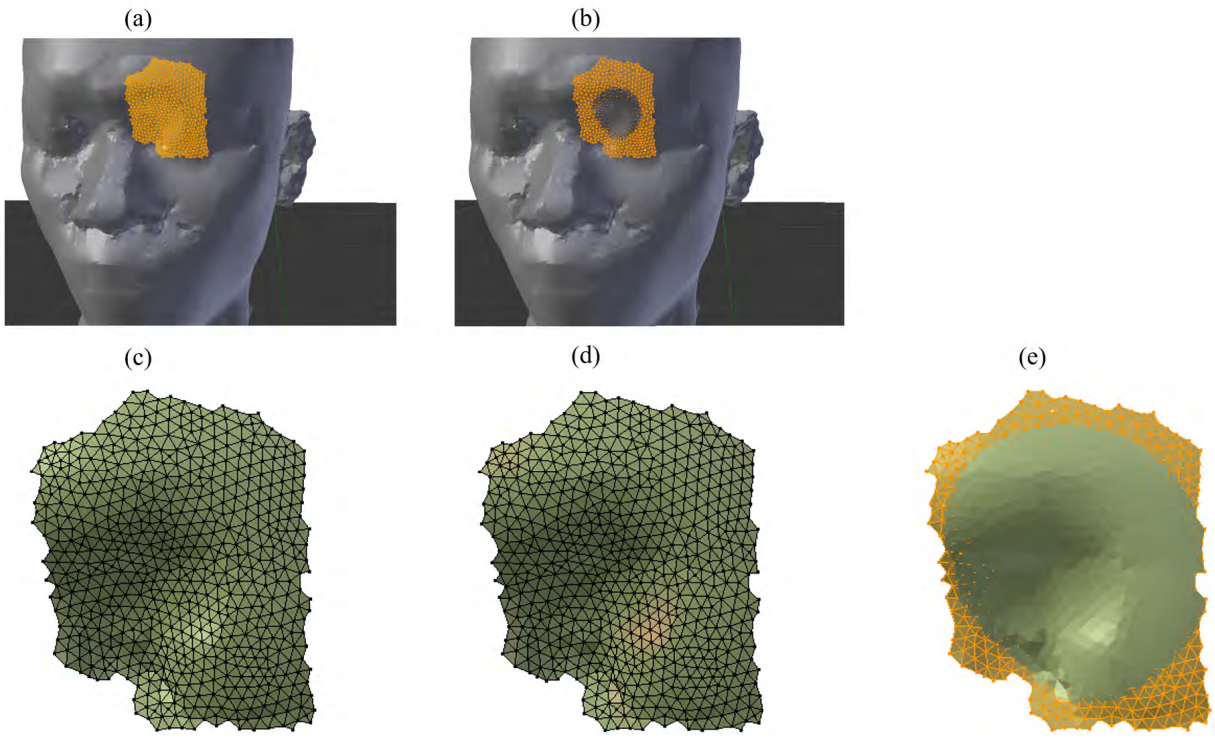

FIGURE 5. Example of skin modeling using mesh grids. (a) Original TARO head model with vertices (in yellow color) of defined skin region number 11, and (b) the modeled skin grid vertices (in yellow color) of overlaid original model. The original external skin region number 11 (c) before and (d) after modeling. (e) Both skin regions in (c) and (d) are overlaid with (c) presented in solid green color and (d) presented in yellow grid points. It is clear that skin thickness is decreased compared to the original one within the region close to the eyelid.

resolution is increased. Memory limitations in commonly available computing facilities may mitigate the production of voxel-based modeling beyond 0.1 mm. An alternative technique is to model the skin using mesh grids that can be used later to generate the voxel model with different resolutions. The smoothed surface polygons of the TARO model are used in this study. First, the external mesh grid is split into the 31 regions (Ω_r, $r = 1, \ldots, 31$) defined in Fig. 1, while the internal mesh grid is unchanged. Here, the term external grid refers to the skin surface that separates anatomical tissue from the outside air region. Given a vertex point $v(i, j, k) \in \Omega_r$, the distance from v to the internal skin mesh grid is computed using the method presented in [26] such that

$$\Delta|_{v(i,j,k)\in\Psi_{out}} = dist(v(i, j, k), \Psi_{in}), \tag{3}$$

where Ψ_{in} and Ψ_{out} are the internal and external mesh grid surfaces of the skin, respectively. The new position of the vertex point v is computed using the following formula:

$$\hat{v} = v + \left[\lambda(\Delta|_v - \bar{t}_r) + (1-\lambda)(\Delta|_v - t_r)\right]\vec{e}, \tag{4}$$

$$\lambda = \left(\frac{dist(v, v_c)}{dist(v_b, v_c)}\right)^2, \tag{5}$$

$$\bar{t}_r = \frac{t_r\, dist(v_b, \tilde{v}_c) + \tilde{t}_r\, dist(v_b, v_c)}{dist(v_c, \tilde{v}_c)} \tag{6}$$

where λ is a weighting parameter, $\bar{t}_r$ is approximated skin width at borders of region Ω_r, v_c and v_b are central and peripheral vertices, respectively, and $\tilde{v}_c$ is a central vertex of a neighbor region with skin thickness $\tilde{t}_r$ as shown in Fig. 4. $\vec{e}$ is a unit vector defining the direction from the point v to the surface Ψ_{in}. The weighting parameter λ is employed to enforce skin smoothness and reliability, especially around the edges of skin sub-regions. The effect of λ is demonstrated in Fig. 4. The skin modeling in (3) is implemented for all 31 skin regions labeled in Fig. 1 to adjust the head skin of the TARO model. An example of modeled skin of region number 11 is shown in Fig. 5.

E. SCALAR POTENTIAL FINITE DIFFERENCE METHOD FOR ELECTROMAGNETIC DOSIMETRY

The scalar potential finite difference (SPFD) method [12] was used for computational dosimetry evaluation. The SPFD method considers a local indexing method with scalar potentials (φ_n) at neighboring labeled nodes ($n = 1, \ldots, 6$) defined with Cartesian coordinates around the target node φ_0. The finite difference equation representing the impedance of applied magnetic field between the nodes can be described as

$$\sum_{n=1}^{6} S_n\varphi_n - \left(\sum_{n=1}^{6} S_n\right)\varphi_0 = j\omega\sum_{n=1}^{6}(-1)^n l^n A_{0n}, \tag{7}$$

where S_n, l_n, ω, and A_{0n} denote the edge conductance derived from the tissue conductivity, the distance between nodes, the angular frequency, and the magnetic vector potential,

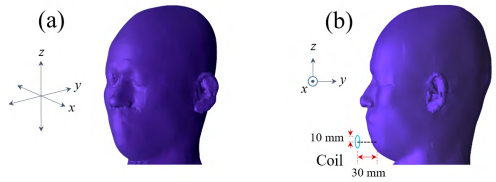

FIGURE 6. Demonstration of exposure scenarios: (a) uniform exposure for LAT (x) and AP (y) directions and (b) a coil of 10 mm radius located 30 mm from chin (simulated electrical shaver).

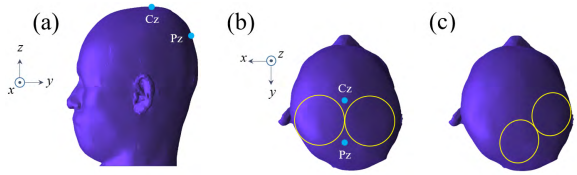

FIGURE 7. Demonstration of TMS coil positioning for brain stimulation. (a) and (b) TMS over mid-way between Cz and Pz, and (c) TMS targeting hand motor area.

respectively. A geometric multigrid method that implements a successive over-relaxation smoothing is detailed in [27] and is used to solve the problem in (7). The solution is found iteratively, and the stopping criterion of the geometric multigrid method for non-uniform exposure is computed for relative residual value of order 10^{-5}, which allows a truncation error of 1% [27]. In the computational results shown in Section III, the stopping criterion for uniform exposure is determined in the same way with residual value of 10^{-6}. The values of S_n assigned to different modeled human tissues in the human head were considered for a four-Cole-Cole dispersion model [28].

F. EXPOSURE SCENARIOS AND EVALUATION METRICS

Two TARO head models, i.e., original model and that with the skin thickness fine-tuned, are considered in a free space. The dosimetry is conducted for exposure to uniform magnetic field in the frontal (AP) and lateral (LAT) directions, as shown in Fig. 6 (a). A magnetic flux density of 0.1 mT at a frequency of 50 Hz is used in both exposure directions. In addition to the maximum value of the *in situ* electric field, the 99.0^{th} to 99.9^{th} percentile values are also computed as surrogates of the maximum value. The computations were conducted over a 2.0 mm average cube. For a non-uniform exposure scenario, a simulated electric shaver is modeled by a one-loop coil with a radius of 10 mm. The center of the coil is located at 30 mm from the chin, as demonstrated in Fig. 6 (b).

G. EXPOSURE SCENARIOS IN MEDICAL APPLICATIONS

The effect of skin modeling is also investigated considering the magnetic field exposure from the TMS coil. Brain stimulation by TMS is applied using a figure-eight coil positioned over the parietal lobe (mid-way between Cz and Pz) and hand motor area, as shown in Fig. 7. A coil current of 1 A with a frequency of 10 kHz is used for both exposure scenarios. The hotspot over the skin is computed as the maximum value of the *in situ* electric field from the 90.0^{th} percentile value for TMS [29].

III. RESULTS AND DISCUSSION

A. SKIN MODELING

The head region is extracted from the original TARO model of 2.0 mm. A polygonized version of the conventional model is generated to represent head segmented regions. The skin modeling is implemented using different resolutions of 0.5, 0.44, 0.25, and 0.22 mm. Both the voxel-based and mesh grid-based approaches described above are implemented to model the head skin regions. We have found a small difference between the two approaches, which corresponds to the accuracy rate of the voxelization process used to generate the final model by the mesh grid-approach. However, computation cost of the skin modeling is considerably increased as we aim for higher resolutions using the voxel-based approach. For this reason and for dosimetry unification, we decided to employ the mesh grid-approach only in the following dosimetry evaluation. The original and resultant Real Skin TARO (RS-TARO) with a resolution of 0.22 mm are shown in Figs. 8 and 9. An example of skin thickness change can be observed within the eyelid region. The skin thickness of the original model reaches a value of 2.2 mm, which is relatively high compared to real measurements. On the other hand, the RS-TARO presents a skin thickness of almost 1.32 mm, which demonstrates a more realistic value, as shown in Fig. 8 (c). Additional examples of skin thickness change are shown in Fig. 9. It is clear from these results that the values of skin thickness, around the forehead, vertex, and chin regions for example, demonstrate a more realistic profile compared with the original high-resolution model.

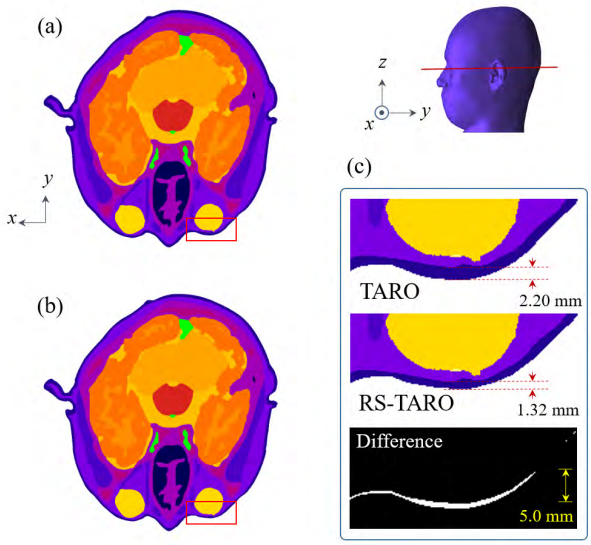

FIGURE 8. Skin modeling results shown in a transverse slice of the TARO head model. (a) High resolution TARO model (0.22 mm) with original skin thickness. (b) RS-TARO with skin modeled using the proposed method (mesh grid-based). (c) Region around eyelid (marked by red rectangle) is magnified to demonstrate the change in skin thickness (around 0.88 mm).

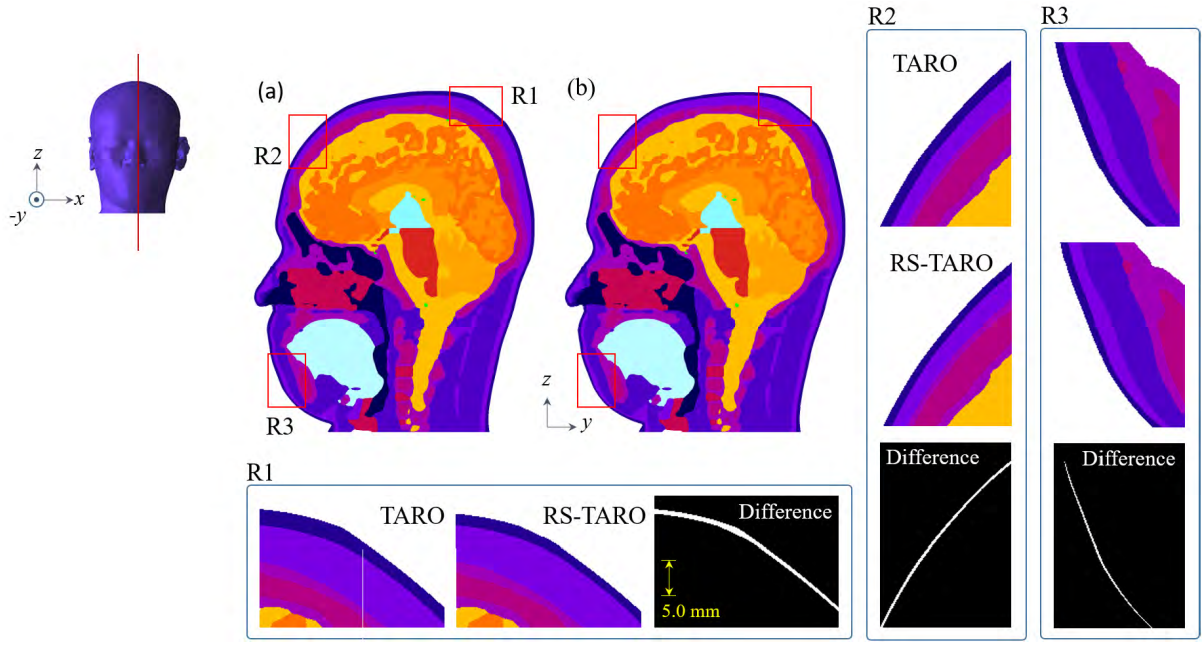

FIGURE 9. Skin modeling results shown in a sagittal slice of the TARO model corresponding to (a) original TARO and (b) RS-TARO (0.22 mm). Regions around the vertex (R1), forehead (R2), and chin (R3) are magnified to demonstrate the change in skin thickness.

B. ELECTROMAGNETIC DOSIMETRY

To discuss the effect of human skin modeling on the *in situ* electric field, we first consider the uniform exposure scenario detailed in Section II.F. The 0.44 mm TARO and RS-TARO head models are exposed to a uniform magnetic field from the AP and LAT directions, and results are computed using the geometric multigrid method. The tissue conductivities used in the dosimetry are shown in Table 2 and are based on the values reported in [20].

Tables 3 and 4 show the *in situ* electric field from the 99.0^{th} to 99.9^{th} percentile value using head models of resolution 0.44 mm. The computed values for all tissues (including skin) and skin only are shown for comparison purposes. From these data, it is clear that the variability of the *in situ* electric field is rather small (5% or less in the 0.44 mm models). This demonstrates that the skin modeling has a small contribution to the distribution of the *in situ* electric field values. For both the LAT and AP directions, consistent variability was observed between the TARO and RS-TARO models. To confirm the effect of model resolution, we repeated the above dosimetry evaluation of uniform exposure using head models of 0.5 and 0.25 mm resolutions. Original dosimetry and 2 mm^3 averaged EF using head models of 0.5 mm (for the LAT and AP directions) are shown in Fig. 9. A comparison of the *in situ* electric field measurements using 0.5 and 0.25 mm for the LAT exposure direction is shown in Fig. 10. These results indicate that the variability of the *in situ* electric field due to the change of model resolution is rather small, except the maximum value. The difference in the maximum value is due to inherent error, which is attributable to the stair-casing discretization in voxel models.

TABLE 2. Human tissue conductivity (S_n) of TARO/RS-TARO head models used with different frequencies.

Tissue	50 Hz	10 kHz	Color label
Skin	0.10	0.1	
Muscle	0.23	0.34	
Fat	0.04	0.04	
Bone (Cortical)	0.02	0.02	
Bone (Cancellous)	0.08	0.08	
Cartilage	0.17	0.18	
Nerve	0.03	0.04	
Grey Matter	0.08	0.10	
White Matter	0.05	0.07	
Cerebellum	0.10	0.13	
CSF	2.00	2.00	
Vitreous Humor	1.50	1.50	
Cornea	0.42	0.44	
Lens	0.32	0.34	
Blood	0.70	0.70	
Tongue	0.27	0.27	
Thalamus	0.09	0.09	

C. ELECTRICAL SHAVER

In the case of the electric shaver, the distribution of the electric field is shown in Fig. 6 (b). The maximum error between the TARO and RS-TARO models (0.5 mm resolution) is lower than 5%, as shown in the data measurements presented in Table 5. The relative difference in electric field distribution is relatively small, as expected considering the skin thickness change values demonstrated in Fig. 9 (R3).

TABLE 3. Maximum voxel value of *in situ* electric field [mV/m] for the LAT exposure direction over different percentile values for original (TARO) and skin modeled (RS-TARO) head models of 0.44 mm resolution.

Percentile	TARO		RS-TARO		Change Rate[%]	
[%]	All	Skin	All	Skin	All	Skin
100	32.8	7.1	32.9	7.4	0.15	4.4
99.9	7.4	5.6	7.5	5.6	0.15	-0.25
99.8	6.5	5.3	6.5	5.3	0.24	-0.21
99.7	5.9	5.1	5.9	5.1	0.25	0.34
99.6	5.6	4.8	5.6	4.9	0.19	1.33
99.5	5.3	4.5	5.3	4.6	0.21	1.85
99.4	5.0	4.3	5.0	4.4	0.23	1.97
99.3	4.7	4.1	4.7	4.2	0.27	1.86
99.2	4.5	3.9	4.5	4.0	0.25	1.79
99.1	4.3	3.7	4.4	3.8	0.23	1.83
99.0	4.2	3.6	4.2	3.7	0.21	1.63

TABLE 4. Maximum voxel value of *in situ* electric field [mV/m] for the AP exposure direction over different percentile values for original (TARO) and skin modeled (RS-TARO) head models of 0.44 mm resolution.

Percentile	TARO		RS-TARO		Change Rate[%]	
[%]	All	Skin	All	Skin	All	Skin
100	21.9	7.6	21.9	7.3	-0.02	-3.82
99.9	5.9	4.0	5.9	4.0	0.08	0.76
99.8	5.1	3.6	5.1	3.6	0.10	0.74
99.7	4.7	3.4	4.7	3.4	0.13	0.44
99.6	4.3	3.3	4.3	3.3	0.14	0.59
99.5	4.1	3.2	4.1	3.2	0.16	0.72
99.4	3.8	3.1	3.8	3.1	0.18	0.62
99.3	3.7	3.0	3.7	3.0	0.15	0.54
99.2	3.5	3.0	3.5	3.0	0.13	0.56
99.1	3.4	2.9	3.4	3.0	0.12	0.49
99.0	3.3	2.9	3.3	2.9	0.11	0.46

TABLE 5. Maximum voxel value of the *in situ* electric field [mV/m] for electric shaver close to chin over different percentile values for the original (TARO) and skin modeled (RS-TARO) head models.

Percentile	TARO		RS-TARO		Change Rate[%]	
[%]	All tissues	Skin	All tissues	Skin	All tissues	Skin
100	1.9	1.2	1.9	1.2	-0.36	1.79
99.9	0.8	1.0	0.8	0.9	1.07	1.58
99.8	0.7	0.9	0.7	0.9	1.16	1.92
99.7	0.6	0.9	0.6	0.9	1.09	2.12
99.6	0.6	0.9	0.6	0.8	1.03	2.33
99.5	0.6	0.8	0.6	0.8	0.93	2.57
99.4	0.5	0.8	0.5	0.8	0.90	2.97
99.3	0.5	0.8	0.5	0.8	0.91	2.96
99.2	0.5	0.8	0.5	0.8	0.94	3.10
99.1	0.5	0.8	0.5	0.7	0.99	3.06
99.0	0.5	0.7	0.4	0.7	1.01	3.14

D. TMS

The TMS exposure scenario is considered for both the original TARO and RS-TRAO head models of 0.22 mm resolution in two stimulation suites. The maximum *in situ* electric field values from the 90.0^{th} to 100th percentiles were computed to obtain the relative difference between both models in three different tissues (skin, fat, and brain), as shown in Fig. 13. Also, the spatial distribution of the electric field strength and relative difference for TMS over the Cz-Pz and hand motor area are shown in Figs. 14 and 15, respectively. The maximum relative difference for stimulation over the Cz-Pz position is 11.0%, 4.1%, and 2.3% for skin, fat, and brain, respectively. Meanwhile, the maximum relative difference is 7.6%, 6.5%, and 4.3% for skin, fat, and brain, for the stimulation of the hand motor area, respectively. These results demonstrate a relatively small variability in internal tissues, while relatively higher values can be observed on the skin

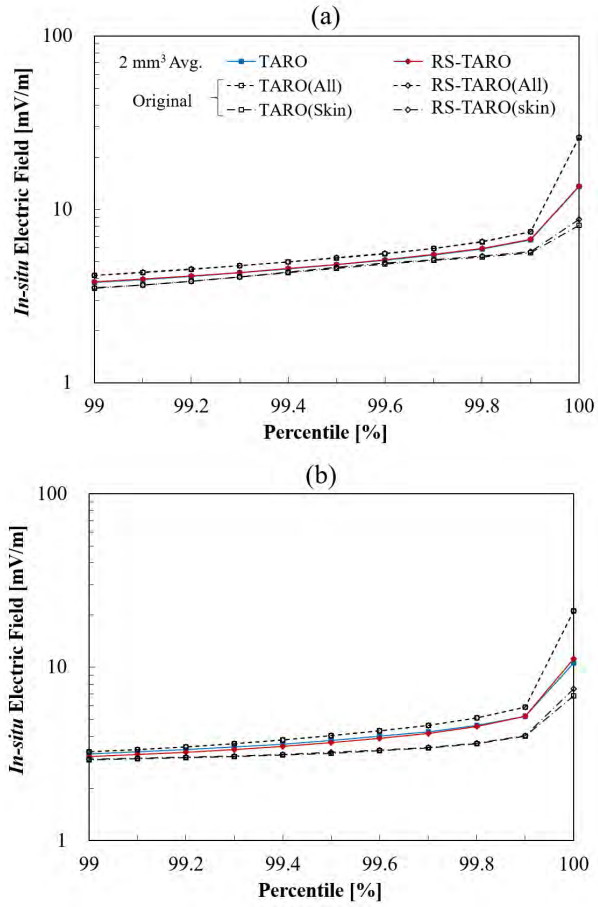

FIGURE 10. Original maximum and averaged voxel values of the *in situ* electric field [mV/m] for (a) LAT and (b) AP exposure directions of TARO and RS-TARO head models (0.5 mm resolution) over different percentile values.

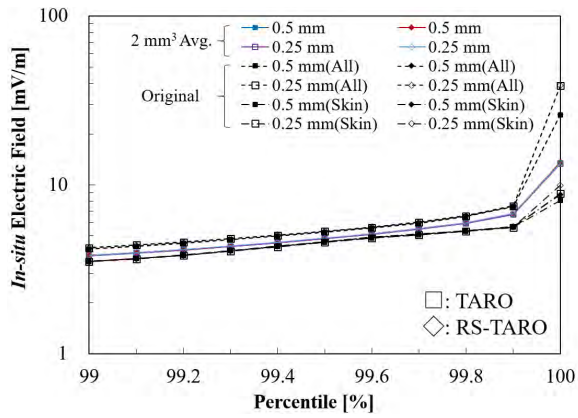

FIGURE 11. Original maximum and averaged voxel values of the *in situ* electric field [mV/m] for LAT exposure direction of TARO and RS-TARO head models (0.25 and 0.5 mm resolutions) over different percentile values.

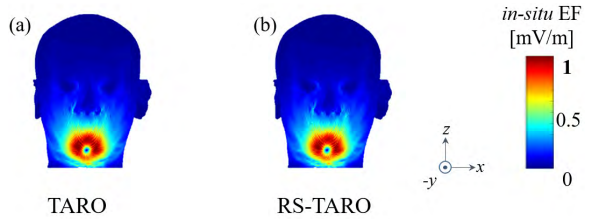

FIGURE 12. Electric field distribution for magnetic exposure of an electric shaver applied to the chin using the (a) TARO and (b) RS-TARO head models.

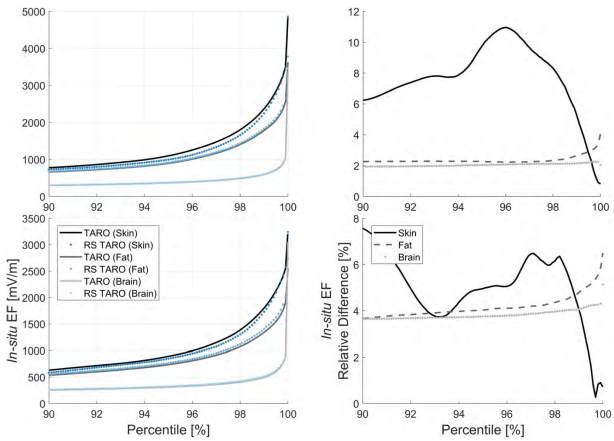

FIGURE 13. *In situ* electric field (left) and relative difference (right) in electric field values for skin, fat, and brain tissues for TMS exposure on two sites: Cz-Pz (top) and hand motor area (bottom).

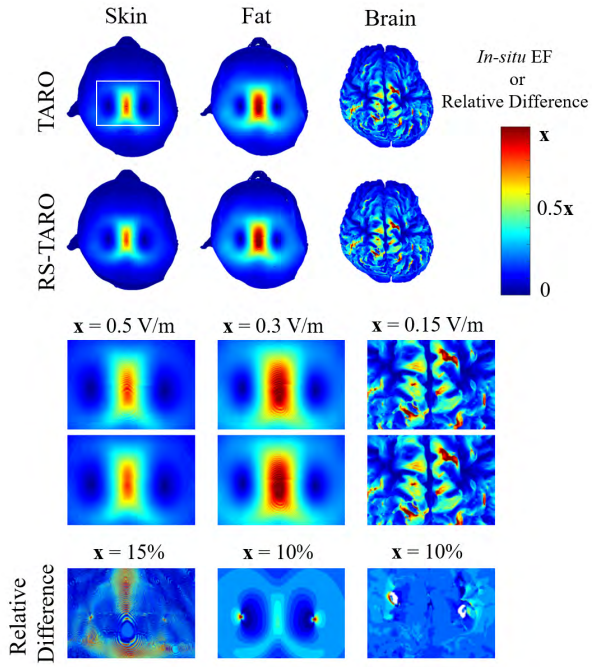

FIGURE 14. TMS electric field distribution for Cz-Pz exposure at skin, fat, and brain tissues in TARO and RS-TARO. Region labed with while rectangle is shown below along with the relative difference in the bottom panel for each tissue.

surface. However, considering the side effect or unwanted stimulation of the skin during the brain stimulation, this difference may not be negligible for clinical planning.

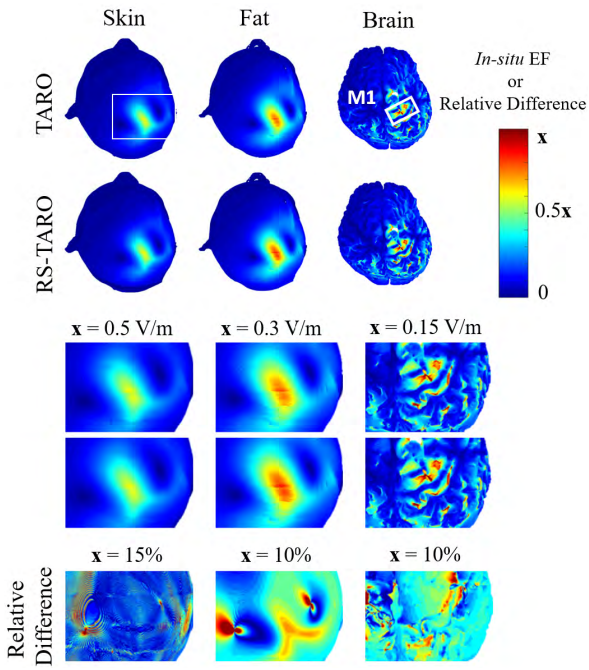

FIGURE 15. TMS electric field distribution for M1 exposure at skin, fat, and brain tissues in TARO and RS-TARO. Region labed with while rectangle is shown below along with the relative difference in the bottom panel for each tissue. M1: hand motor area.

IV. CONCLUSION

The use of human models with detailed skin modeling becomes essential in LF dosimetry. Generation of high-resolution human models using low resolution ones may lead to inappropriate skin thickness. In this study, we developed two different methods for modeling skin thickness so that it more closely represents real measurements. Voxel- and mesh grid-based methods were proposed for accurate skin modeling. Results indicated that the proposed methods were effective in producing more realistic models with high quality.

We then investigated the variation of electric field distribution in human models due to skin modeling. We considered different exposure scenarios: uniform magnetic field exposure, TMS, and canonical electrical shaver. Results indicated that the effect of skin modeling for uniform exposure (from either the LAT or AP direction) is fairly small with a maximum variability of 5%. Almost the same value can be confirmed with the simulation of an electrical shaver. However, a relatively higher variability of more than 11% can be observed with medical applications such as TMS.

For future work, it would be interesting to conduct additional computational/experimental dosimetry to validate the effect of skin modeling for TMS and investigate side effects such as pain in cranial nerves.

ACKNOWLEDGMENT

The authors would like to thank Mr. K. Aga (Nagoya Institute of Technology, Nagoya, Japan) for his help with the uniform exposure computations.

REFERENCES

[1] A. Ahlbom *et al.*, "Guidelines for limiting exposure to time-varying electric, magnetic, and electromagnetic fields (up to 300 GHz)," *Health Phys.*, vol. 74, no. 4, pp. 494–521, 1998.

[2] *Standard for Safety Levels With Respect to Human Exposure to Radio Frequency Electromagnetic Fields, 3 kHz to 300 GHz*, IEEE Standard C95.6, 2002.

[3] J. P. Reilly and A. Hirata, "Low-frequency electrical dosimetry: Research agenda of the ieee international committee on electromagnetic safety," *Phys. Med. Biol*, vol. 61, no. 12, p. R138, 2016.

[4] S. Rossi, M. Hallett, P. M. Rossini, and A. Pascual-Leone, "Safety, ethical considerations, and application guidelines for the use of transcranial magnetic stimulation in clinical practice and research," *Clin. Neurophys.*, vol. 120, no. 12, pp. 2008–2039, Dec. 2009.

[5] V. De Santis, X. L. Chen, I. Laakso, and A. Hirata, "An equivalent skin conductivity model for low-frequency magnetic field dosimetry," *Biomed. Phys. Eng. Express*, vol. 1, no. 1, 2015, Art. no. 015201.

[6] J. Motogi *et al.*, "Why intra-epidermal electrical stimulation achieves stimulation of small fibres selectively: A simulation study," *Phys. Med. Biol.*, vol. 61, no. 12, pp. 4479–4490, 2016.

[7] C. Li and T. Wu, "Dosimetry of infant exposure to power-frequency magnetic fields: Variation of 99th percentile induced electric field value by posture and skin-to-skin contact," *Bioelectromagnetics*, vol. 36, no. 3, pp. 204–218, 2015.

[8] G. Schmid, S. Cecil, and R. Überbacher, "The role of skin conductivity in a low frequency exposure assessment for peripheral nerve tissue according to the ICNIRP 2010 guidelines," *Phys. Med. Biol.*, vol. 58, no. 13, pp. 4703–4716, 2013.

[9] S. Fiocchi, E. Chiaramello, M. Parazzini, and P. Ravazzani, "Influence of tissue conductivity on foetal exposure to extremely low frequency magnetic fields at 50 Hz using stochastic dosimetry," *PloS One*, vol. 13, no. 2, 2018, Art. no. e0192131.

[10] R. Kavet, "Dosimetric uncertainties: Magnetic field coupling to peripheral nerve," *Health Phys.*, vol. 109, no. 6, pp. 556–565, 2015.

[11] M.-C. Gosselin *et al.*, "Development of a new generation of high-resolution anatomical models for medical device evaluation: The virtual population 3.0," *Phys. Med. Biol.*, vol. 59, no. 18, pp. 5287–5303, 2014.

[12] T. W. Dawson and M. A. Stuchly, "Analytic validation of a three-dimensional scalar-potential finite-difference code for low-frequency magnetic induction," *Appl. Comput. Electromagnet. J.*, vol. 11, pp. 72–81, Nov. 1996.

[13] K. Chopra *et al.*, "A comprehensive examination of topographic thickness of skin in the human face," *Aesthetic Surg. J.*, vol. 35, no. 8, pp. 1007–1013, 2015.

[14] J. G. B. Derraik *et al.*, "Effects of age, gender, BMI, and anatomical site on skin thickness in children and adults with diabetes," *PloS One*, vol. 9, 2014, Art. no. e86637.

[15] P. U. Giacomoni, T. Mammone, and M. Teri, "Gender-linked differences in human skin," *J. Dermatological Sci.*, vol. 55, no. 3, pp. 144–149, 2009.

[16] M. Alper, A. Kavak, A. H. Parlak, R. Demirci, I. Belenli, and N. Yesildal, "Measurement of epidermal thickness in a patient with psoriasis by computer-supported image analysis," *Braz. J. Med. Biol. Res.*, vol. 36, no. 12, pp. 111–117, 2004.

[17] J. Sandby-Moller, T. Poulsen, and H. C. Wulf, "Epidermal thickness at different body sites: Relationship to age, gender, pigmentation, blood content, skin type and smoking habits," *Acta Dermato Venereologica*, vol. 83, no. 6, pp. 410–413, 2003.

[18] Y. Lee and K. Hwang, "Skin thickness of Korean adults," *Surgical Radiol. Anatomy*, vol. 24, pp. 183–189, Aug./Sep. 2002.

[19] T. M. Bücking, E. R. Hill, J. L. Robertson, E. Maneas, A. A. Plumb, and D. I. Nikitichev, "From medical imaging data to 3D printed anatomical models," *PloS one*, vol. 12, no. 5, 2017, Art. no. e0178540.

[20] T. Nagaoka and S. Watanabe, "Voxel-based variable posture models of human anatomy," *Proc. IEEE*, vol. 97, no. 12, pp. 2015–2025, Dec. 2009.

[21] K. Taguchi, T. Kashiwa, and A. Hirata, "Development on high resolution human voxel model for high frequency exposure analysis," Presented at the Progr. Electromagn. Res. Symp., Toyama, Japan, 2018.

[22] P. Milanfar, *Super-Resolution Imaging*. Boca Raton, FL, USA: CRC Press, 2010.

[23] T. Nagaoka *et al.*, "Development of realistic high-resolution whole-body voxel models of Japanese adult males and females of average height and weight, and application of models to radio-frequency electromagnetic-field dosimetry," *Phys. Med. Biol.*, vol. 49, no. 1, pp. 1–15, 2004.

[24] L. I. Rudin, S. Osher, and E. Fatemi, "Nonlinear total variation based noise removal algorithms," *Phys. D, Nonlinear Phenomena*, vol. 60, nos. 1–4, pp. 259–268, 1992.

[25] A. Chambolle, "An algorithm for total variation minimization and applications," *J. Math. Imag. Vis.*, vol. 20, no. 1, pp. 89–97, 2004.

[26] D. Maier, J. Hesser, and R. Manner, "Fast and accurate closest point search on triangulated surfaces and its application to head motion estimation," in *Proc. 3rd WSEAS Int. Conf. Signal, Speech Image Process.*, 2003. [Online]. Available: http://www.cvl.iis.u-tokyo.ac.jp/~oishi/Papers/Alignment/maier-Fast_Robust_ICOSSIP2003.pdf

[27] I. Laakso and A. Hirata, "Fast multigrid-based computation of the induced electric field for transcranial magnetic stimulation," *Phys. Med. Biol.*, vol. 57, no. 23, pp. 7753–7765, 2012.

[28] S. Gabriel, R. W. Lau, and C. Gabriel, "The dielectric properties of biological tissues: III. Parametric models for the dielectric spectrum of tissues," *Phys. Med. Biol.*, vol. 41, no. 11, pp. 2271–2293, 1996.

[29] S. Aonuma *et al.*, "A high-resolution computational localization method for transcranial magnetic stimulation mapping," *NeuroImage*, vol. 172, pp. 85–93, May 2018.

ESSAM A. RASHED (S'07–M'11) received the B.Sc. degree in scientific computing and the M.Sc. degree in computer science from Suez Canal University, Ismailia, Egypt, in 1998 and 2002, respectively, and the Ph.D. degree in computer science from the University of Tsukuba, Tsukuba, Japan, in 2010. From 2010 to 2012, he was a Research Fellow of the Japan Society for the Promotion of Science (JSPS), University of Tsukuba, Japan. He served as an Assistant Professor with the Department of Mathematics, Faculty of Science, Suez Canal University, from 2012 to 2016. Since 2016, he has been an Associate Professor with Suez Canal University, Egypt, and also with The British University in Egypt (on Secondment). He is currently a Research Associate Professor with the Nagoya Institute of Technology. His research interests include medical image processing, data analysis and visualization, deep learning, and pattern recognition. He is a member of JSPSAAE. He was a recipient of the Egyptian National Doctoral Scholarship, in 2006, JSPS Postdoctoral Fellowship, in 2010, JAMIT Best Presentation Award, from 2008 to 2012, and the Chairman Award, the Department of Computer Science, University of Tsukuba, in 2010. He served as a PI for several projects funded from Science and Technology Development Fund (STDF), Egypt.

JOSE GOMEZ-TAMES (S'13–M'17) was born in Cartago, Costa Rica. He received the B.S. degree in electronics engineering from the Institute of Technology of Costa Rica, Cartago, in 2007, and the M.S and Ph.D. degrees in medical system engineering from Chiba University, Chiba, Japan, in 2012 and 2015, respectively.

From 2007 to 2009, he was an Instructor with the Institute of Technology of Costa Rica. From 2015 to 2016, he was a Research Fellow of the Japan Society for the Promotion of Science, in 2015. Since 2016, he has been a Research Assistant Professor and subsequently a Research Associate Professor with the Nagoya Institute of Technology. He has authored more than 50 papers published in international journals and conference proceedings. His researches focus on computational bioelectromagnetics, neural engineering, and their biomedical applications.

Dr. Gomez-Tames was a recipient of the Monbukagakusho Research Scholarship, JSPS Postdoctoral Fellowship, and the Young Scientist Award in URSI General Assembly and Scientific Symposium, Montreal, Canada, in 2017. He is the Working Group Chair of subcommittee of EMF Dosimetry Modeling of the IEEE International Committee on Electromagnetic Safety and a member of the Scientific Expert Group of the International Commission on Non-Ionizing Radiation Protection.

AKIMASA HIRATA (S'98–M'01–SM'10–F'17) received the B.E., M.E., and Ph.D. degrees in communications engineering from Osaka University, Suita, Japan, in 1996, 1998, and 2000, respectively.

From 1999 to 2001, he was a Research Fellow of the Japan Society for the Promotion of Science, and also a Visiting Research Scientist with the University of Victoria, Victoria, BC, Canada, in 2000. In 2001, he joined the Department of Communications Engineering, Osaka University, as an Assistant Professor. In 2004, he joined, as an Associate Professor with the Department of Computer Science and Engineering, Nagoya Institute of Technology, where he is currently a Full Professor. His research interests include electromagnetic safety, risk management system for heat-related illness, methods in neuroscience, antennas, filters, and related computational techniques.

Dr. Hirata is a Fellow of the Institute of Physics, and a member of IEICE, IEE Japan, and Bioelectromagnetics Society. He is an Editorial Board Member of *Physics in Medicine and Biology* and a member of the main commission. He received several awards including Young Scientists' Prize, in 2006 and Prizes for Science and Technology (Research Category 2011 and Public Understanding Promotion Category 2014) by the Commendation for Science and Technology by the Minister of Education, Culture, Sports, Science, and Technology, Japan, and IEEE EMC-S Technical Achievement Award, in 2015, and the Japan Academy Medal and JSPS Prize, in 2018. He is a Chair of project group of the International Commission on Non-Ionizing Radiation Protection, a member of administrative committee and a Subcommittee (EMF Dosimetry Modeling) Chair of the IEEE International Committee on Electromagnetic Safety, and an Expert of World Health Organization. From 2006 to 2012, he was also an Associate Editor of the IEEE Transactions on Biomedical Engineering.